High-quality quantum chemical data for spin state determination in transition-metal complexes

Mandira Dey,[†,§] Anuj Kumar Ray,[†,§] Vic Austen,[‡,§] Quan Manh Phung,[*,‡,¶] Takeshi Yanai,[*,‡,¶] Ankan Paul,[*,†] and Debashree Ghosh[*,†]

†*School of Chemical Sciences, Indian Association for the Cultivation of Science, Kolkata, India*

‡*Department of Chemistry, Graduate School of Science, Nagoya University, Furo-cho, Chikusa-ku, Nagoya, Aichi 464-8602, Japan*

¶*Institute of Transformative Bio-Molecules (WPI-ITbM), Nagoya University, Furo-cho, Chikusa-ku, Nagoya, Aichi 464-8601, Japan*

§*Equal contribution*

E-mail: quan.phung@chem.nagoya-u.ac.jp; yanait@chem.nagoya-u.ac.jp; rcap@iacs.res.in; pcdg@iacs.res.in

Active Space of CASPT2 Calculations

The active space of the CASPT2 calculations includes three groups of orbitals (Figure S1). The first group, which is always included in the active space, consists of two metal-ligand bonding orbitals: one involving the metal $3d_{z^2}$ orbital and the two axial ligands (denoted $\sigma_{LBO(z^2)}$), and the other involving the $3d_{x^2-y^2}$ orbital and the four equatorial ligands (denoted $\sigma_{LBO(x^2-y^2)}$). The second group, also always included, consists of the five $3d$ ($3d_{xy}$, $3d_{yz}$, $3d_{xz}$, $3d_{x^2-y^2}$ and $3d_{z^2}$) orbitals of the metals. The third group of orbitals consists of a subset of metal $4d$ orbitals to account for the double-shell effect. Specifically, a $4d$ orbital is included

only when the corresponding $3d$ orbital is occupied. Illustrations of these orbitals (on a sample complex, $[Fe(CH_3CN)_6]^{3+}$ in the quintet state) can be found in Figure S1, while active spaces for all complexes considered are provided in Table S1.

Table S1: Active spaces used in CASPT2/CC calculations.

Metal	Oxidation State	$3d$ electrons	Spin multiplicity	Active Space
Cr	+2	4	1	8 in 9
			3	8 in 10
			5	8 in 11
Mn	+2	5	2	9 in 10
			4	9 in 11
			6	9 in 12
	+3	4	1	8 in 9
			3	8 in 10
			5	8 in 11
Fe	+2	6	1	10 in 10
			3	10 in 11
			5	10 in 12
	+3	5	2	9 in 10
			4	9 in 11
			6	9 in 12
Co	+3	6	1	10 in 10
			3	10 in 11
			5	10 in 12

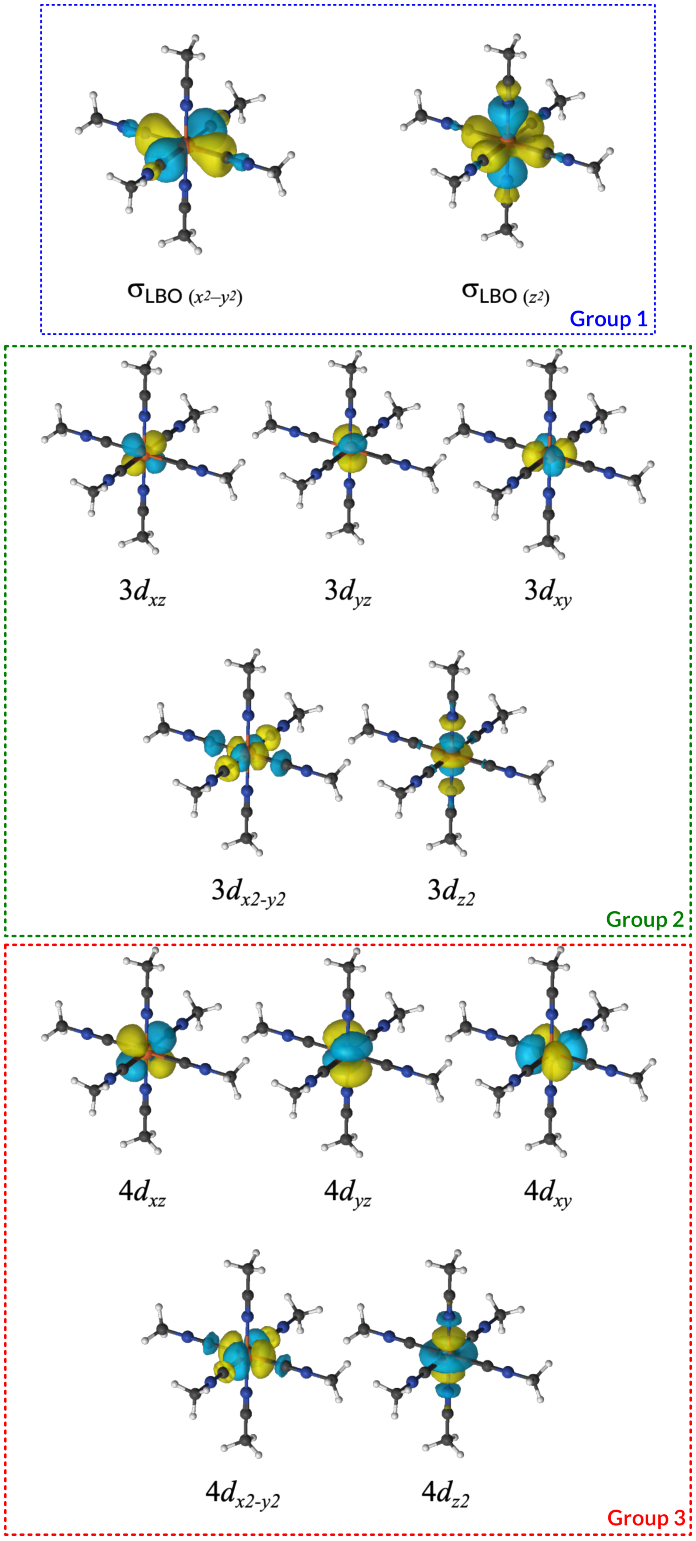

Figure S1: Illustration of the active orbitals, separated into the 3 groups.

CCSD(T)/CBS Calculations

Estimations of CCSD(T)/CBS were obtained using a protocol based on CCSD(T)-F12 proposed by Drabik and Radoń[1], with a slight modification to reduce computational cost. Specifically, instead of performing two expensive CCSD(T) calculations to capture the contribution of scalar relativistic effects through the Douglas–Kroll–Hess (DKH) Hamiltonian, we only performed two low-cost MP2 calculations. The basis sets used are unchanged from the original procedure. The final CCSD(T)/CBS relative energy is then calculated by

$$\Delta E_{\mathrm{CCSD(T)/CBS}} = \Delta E_{\mathrm{CCSD(T\#)-F12a}} + \Delta E_{\mathrm{MP2}}(+\mathrm{DKH}) - \Delta E_{\mathrm{MP2}}(\mathrm{noDKH}),$$

where $\Delta E_{\mathrm{MP2}}(+\mathrm{DKH})$ and $\Delta E_{\mathrm{MP2}}(\mathrm{noDKH})$ represent the relative energies from the MP2 calculations with and without DKH relativistic effects, respectively. The relative energies of the spin states of five complexes were calculated using this protocol. The results, along with CASPT2/CC results, are shown in Table S2.

Table S2: Relative energies calculated using CCSD(T#)-F12a, CCSD(T)/CBS and CASPT2/CC. All values are in kcal/mol.

Complex	Spin multiplicity	$\Delta E_{\mathrm{CCSD(T\#)-F12a}}$	$\Delta E_{\mathrm{CCSD(T)/CBS}}$	$\Delta E_{\mathrm{CASPT2/CC}}$
$[Cr^{II}(NH_3)_4(CN)_2]$	1	45.1	43.6	44.0
	3	13.1	11.7	11.9
	5	0.0	0.0	0.0
$[Fe^{II}(H_2O)_5Cl]^+$	1	29.6	29.6	33.4
	3	28.6	28.6	30.0
	5	0.0	0.0	0.0
$[Fe^{III}(NH_3)_5(CH_3NC)]^{2+}$	2	3.2	3.1	1.8
	4	14.8	15.3	14.8
	6	0.0	0.0	0.0
$[Mn^{II}(NH_3)_4(CN)_2]$	2	34.2	31.4	32.7
	4	28.3	26.5	27.5
	6	0.0	0.0	0.0
$[Mn^{III}(NH_3)_5(CH_3CN)]^{2+}$	1	47.1	46.1	41.4
	3	11.1	10.4	6.1
	5	0.0	0.0	0.0

Details of electronic property-based descriptor

The input descriptors were designed based on electronic properties or molecular orbitals of the highest spin state (within the 3d orbitals) of the system. Since the high spin state is expected to show the minimal effects of multireference nature, these orbitals are expected to be more chemically important. This is the reasoning behind the descriptor pool creation.

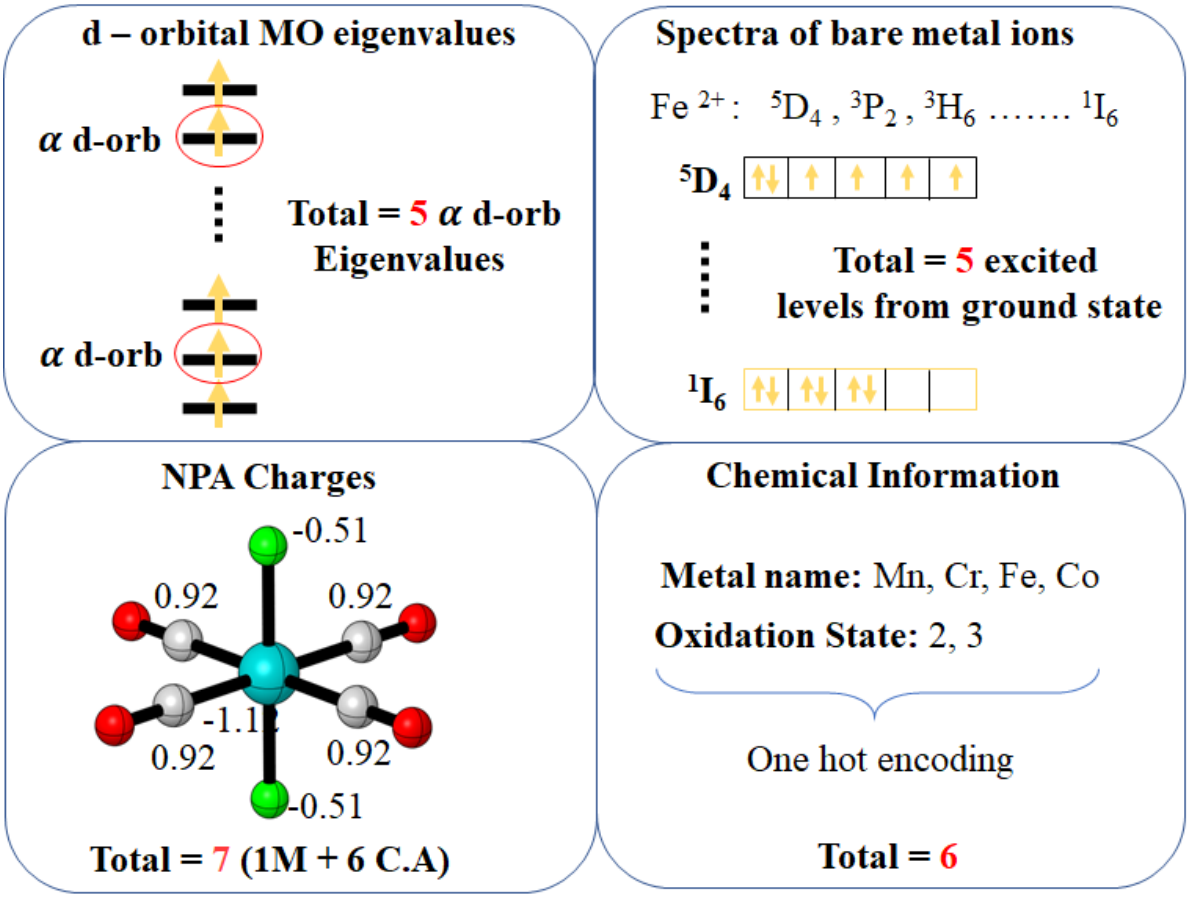

Figure S2: Overview of the description of electronic property-based input descriptor Des-δ. The total descriptor vector size is 23.

Fig. S2 shows the description of the electronic property-based input descriptor Des-δ. The 5 metal 3d orbitals (with α spin) in the highest spin state are included. This is expected to introduce information about the crystal field splitting. The atomic spectra of the specific metal center are included to introduce information about the metal in that specific oxidation state. The NPA charges on the metal center and the nearest neighbor atoms of the ligand

provide information about the electronegativity difference. Finally, the name and oxidation state of the metal are also included in the input descriptor vector. The total input descriptor vector length is 23. Each of the sets of descriptors is explained in detail with examples below.

One-hot encoded chemical information

Table S3: One-hot encoding of metal names.

Metal name	Encoding
Mn	1 0 0 0
Cr	0 1 0 0
Fe	0 0 1 0
Co	0 0 0 1

Table S4: One-hot encoding of the oxidation state of the metal center.

Oxidation	Encoding
2	1 0
3	0 1

α d-orbital energies

D component of MO coefficients corresponding to the orbitals

Orbital energies --	-0.16657	-0.16642	-0.15628	-0.15439	-0.15434
9D 0	0.00033	-0.00094	0.00062	-0.01401	-0.00705
9D+1	-0.03320	0.00843	-0.00865	-0.27628	0.34695
9D-1	-0.03057	0.01189	0.00369	0.34836	0.26721
9D+2	0.00185	-0.00013	0.48323	-0.00781	0.00625
9D-2	-0.00065	-0.00001	0.01481	-0.00571	0.00617
10D 0	0.00015	-0.00034	0.00026	-0.00518	-0.00260
10D+1	-0.01237	0.00281	-0.00314	-0.10226	0.12845

```
10D-1                    -0.01135   0.00423   0.00134   0.12895   0.09893
10D+2                     0.00068  -0.00004   0.17445  -0.00286   0.00225
10D-2                    -0.00025   0.00001   0.00535  -0.00243   0.00247
-------------------------------------------------------------------------
Total D contribution:    -0.08538   0.02591   0.67195   0.06076   0.84902
```

Five orbitals having the largest D contribution were taken as d-orbitals.

Natural charges

Complex's name is represented in this way:

metal_oxidation_equatorial_equatorial_equatorial_equatorial_axial_axial_s_spin

The NPA charges for the complex "co_2_cyanide_cyanide_cyanide_cyanide_ammonia_ammonia_s_5" have been arranged as

$$[0.44118, 0.03433, 0.03190, 0.03605, 0.03382, -1.00141, -1.00153]$$

The first one is for metal, and the other 6 are for coordinating atoms.

Atomic spectra

Table S5: B3LYP/def2-TZVP calculated 5 lowest excited energies of bare metal ions.

Metal	Lowest five atomic levels (a.u.)				
Mn^{2+}	0.11580	0.19319	1.87022	4.11301	6.57206
Mn^{3+}	0.10343	0.19645	1.58054	3.70998	6.25893
Cr^{2+}	0.05187	0.12605	1.41254	3.08739	5.11107
Cr^{3+}	0.09233	1.44015	2.85727	4.78161	8.05548
Fe^{2+}	0.09143	0.14409	0.16950	2.66400	5.35253
Fe^{3+}	0.13898	0.23184	2.35643	5.15834	8.18735
Co^{2+}	0.08366	0.22506	0.84372	3.81577	7.03570
Co^{3+}	0.10755	0.16999	0.46910	3.53593	6.84866

Error analysis of four descriptor sets

To build an ML protocol for predicting spin gaps of TM complexes, we propose the construction of electronic property-based descriptors that effectively capture the coordination environment of the metal centers, enabling a unique and informative representation of each complex. These descriptors are derived from orbital and allied electronic structure information through low-cost quantum chemical calculations. We have evaluated four descriptors built around these principles referred to as Des-α, Des-β, Des-γ, and Des-δ.

The Des-α comprises (a) metal name and (b) metal oxidation state in one-hot encoded form, (c) energies (in a.u.) of five alpha and five beta valence orbitals of high-spin state calculated at B3LYP/def2-TZVP level of theory, (d) natural charges (in a.u.) on the metal center, and the coordinating atoms, and (e) the energies (in a.u.) of the lowest ten electronic states of the bare metal ion.

In Des-β, instead of using valence orbitals, we include the energies of five α and five β $3d$-orbitals from the high-spin state. Furthermore, from this descriptor onward, we have used two separate models to predict the energy gaps between high-spin and intermediate-spin states ($\Delta E_{\mathrm{HI}} = E_{\mathrm{HS}} - E_{\mathrm{IS}}$) and intermediate-spin and low-spin states ($\Delta E_{\mathrm{IL}} = E_{\mathrm{IS}} - E_{\mathrm{LS}}$). In Des-$\gamma$, we have further noticed that the energies of the α and β orbitals are quite correlated, and therefore, we have only taken the energies of the five α $3d$-orbitals, thus reducing the total size of the descriptor. Finally, the Des-δ contains five α $3d$-orbital energies, NPA-calculated charges of the metal and its six coordinating atoms, five lowest electronic state energies of bare metal ion, the metal names, and the oxidation number. The orbital energies and natural charges are computed at B3LYP/def2-SVP level of theory. This choice aligns with our goal of enabling high-throughput screening by relying on affordable quantum chemical calculations. The sizes of these descriptors are 33, 33, 28, and 23, respectively. We have tested the relative errors obtained with all these descriptors for the prediction of spin gaps at the B3LYP/def2-TZVP level of theory.

Fig. S3 shows the mean absolute errors (MAEs) of four descriptor sets–Des-α, β, γ

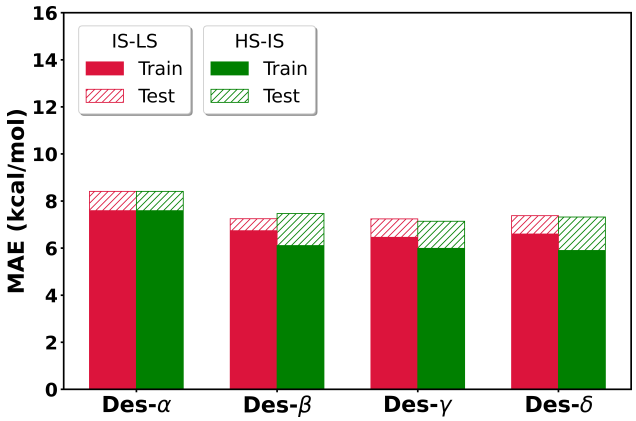

Figure S3: Comparison of MAEs (in kcal/mol) for ΔE_{HI} and ΔE_{IL} predictions across four descriptor sets using a LASSO model.

and δ–in predicting spin energy gaps (ΔE_{HI} and ΔE_{IL}) of monometallic TM complexes. A LASSO regression model was used to evaluate the performance of each descriptor set. An improvement of MAE was observed from Des-α to β, highlighting the importance of including 3d-orbital energies as descriptors over general valence orbital energies. While the errors obtained with Des-β and γ are comparable, the latter is more favorable, since it is more compact by including only 3d α-orbital energies. Notably, Des-δ also exhibits a similar accuracy to Des-γ while having the same descriptor size, but with the advantage of being derived from low-cost B3LYP*/def2-SVP calculations. Based on the balance of accuracy, compactness, and computational cost, we selected Des-δ as the descriptor set of choice for all subsequent analyses in this study.

Error analysis of different regression models

Figures S4–S7 show the training and testing mean absolute errors (MAEs) in kcal/mol for the spin gaps (ΔE_{IL} and ΔE_{HI}). Note that these errors are prior to extensive tuning of hyperparameters and show that the predictive accuracy can vary significantly across different regression models. The performance of the optimized regression model and the final model used in this work are reported in the main manuscript.

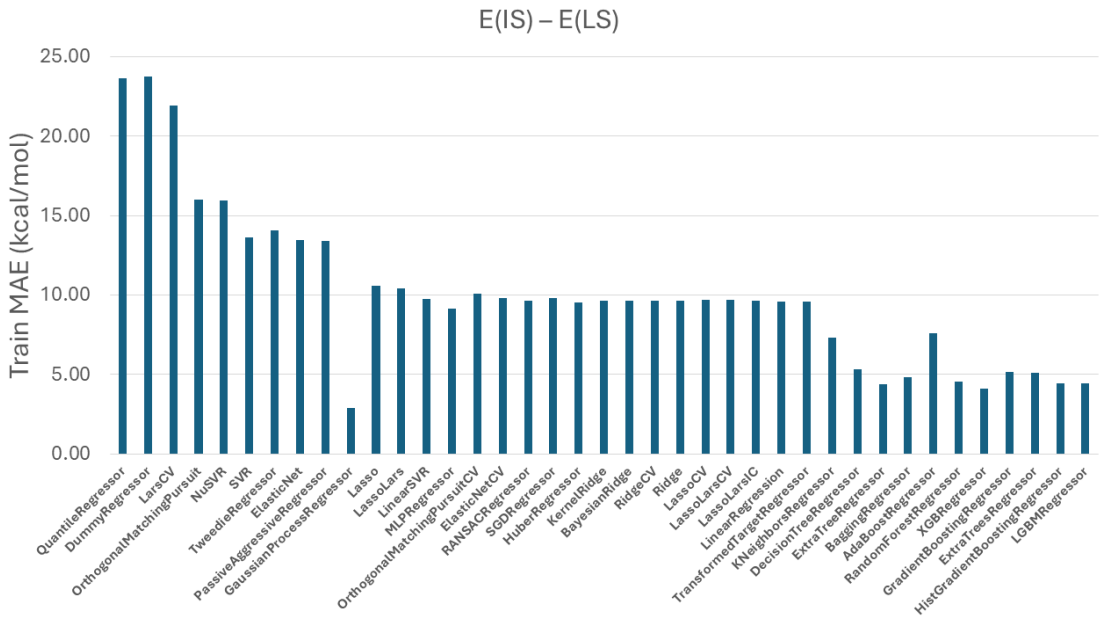

Figure S4: Train MAE (in kcal/mol) of ΔE_{IL} using different ML models.

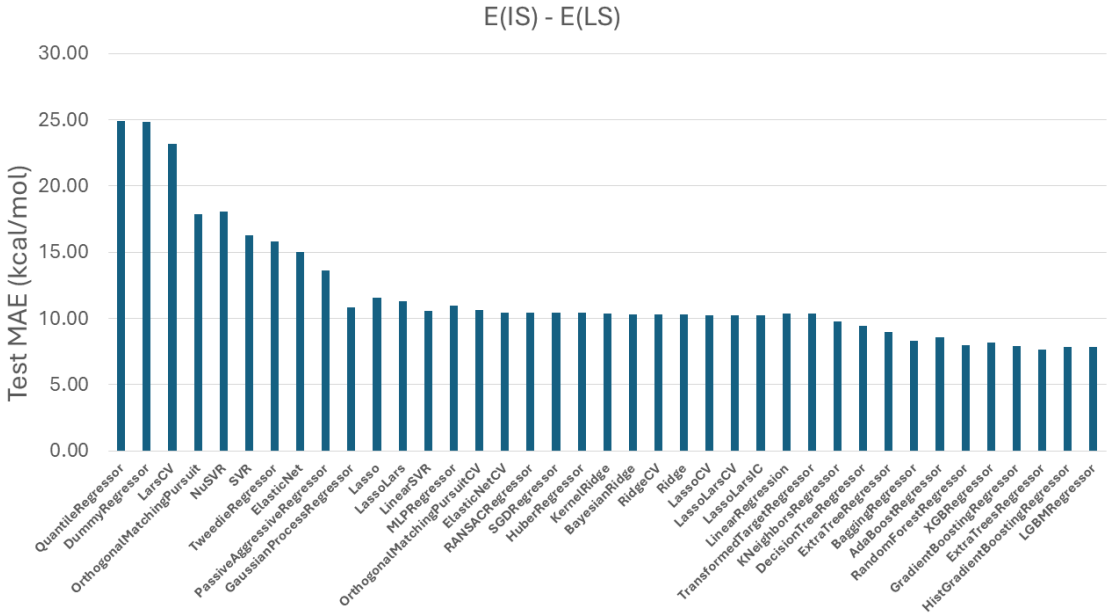

Figure S5: Test MAE (in kcal/mol) of ΔE_{IL} using different ML models.

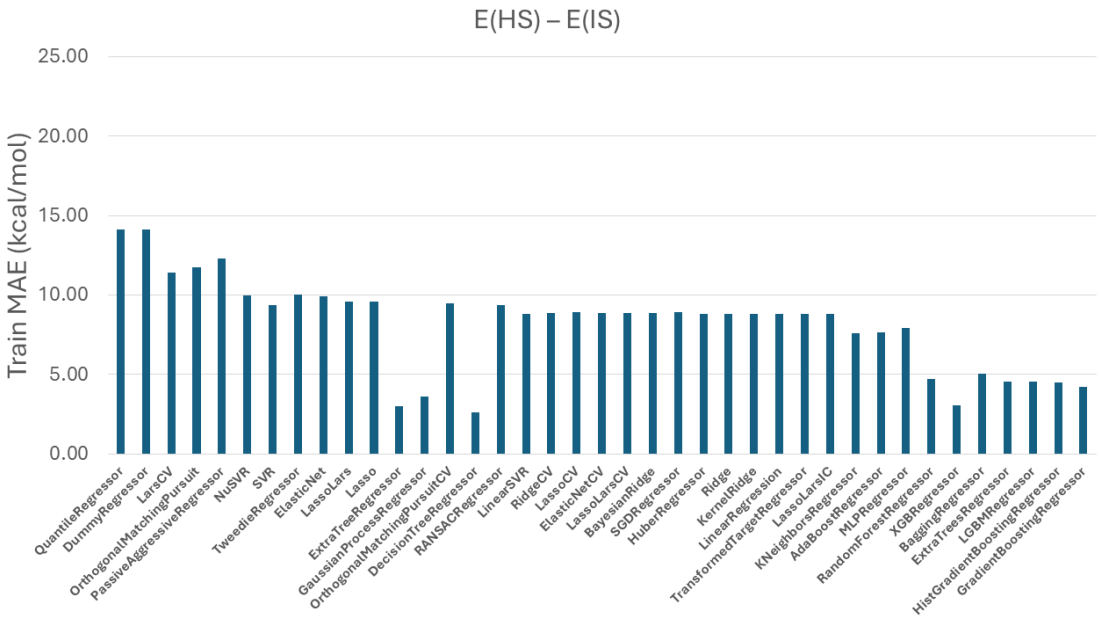

Figure S6: Train MAE (in kcal/mol) of ΔE_{HI} using different ML models.

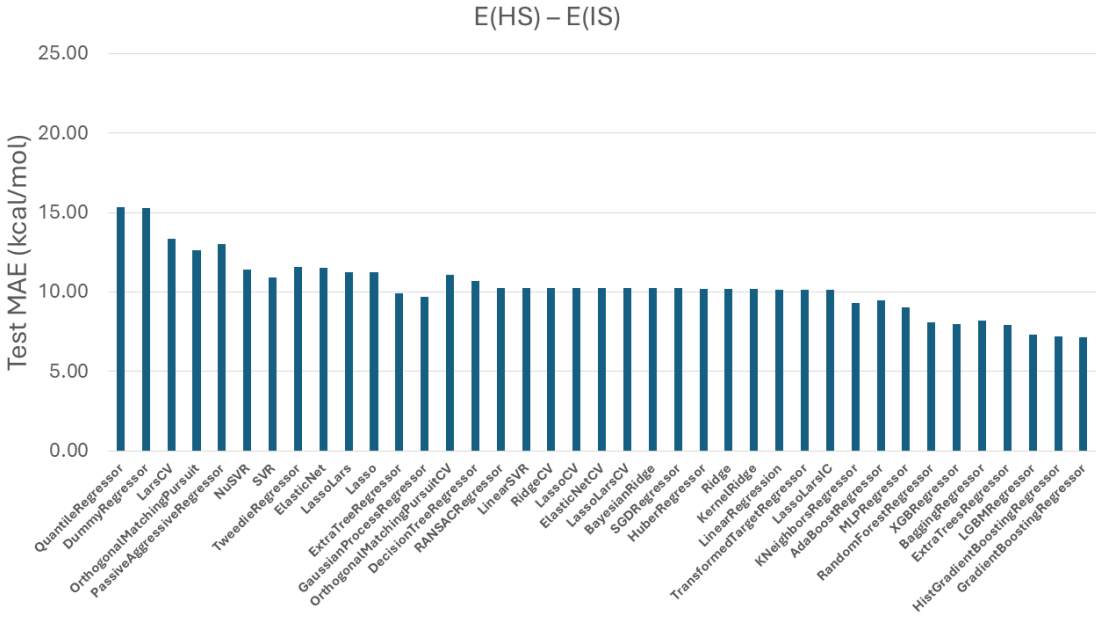

Figure S7: Test MAE (in kcal/mol) of ΔE_{HI} using different ML models.

Error of KRR with different kernels

Different kernel functions were tested such as linear, polynomial, Laplacian, and Gaussian. The MAE errors corresponding to the kernels are shown in Table S6.

Table S6: MAE errors of the KRR model for training and testing the adiabatic ΔE_{HI} and ΔE_{IS} gap with different kernel functions. MAEs are in kcal/mol.

Kernel function	ΔE_{HI}		ΔE_{IS}	
	Train MAE	Test MAE	Train MAE	Test MAE
Gaussian	2.52	5.60	4.06	5.50
Laplacian	1.09	3.95	0.99	4.80
Linear	5.91	7.32	6.61	7.35
Polynomial/ Degree 2	4.53	5.71	5.08	6.10
Polynomial/ Degree 3	4.56	5.69	4.25	5.77

Distribution of B3LYP/def2-TZVP calculated adiabatic ΔE_{HI} and ΔE_{IL} gaps

The distributions of the calculated spin gaps at the B3LYP/def2-TZVP level are shown for the different metal centers. These distributions highlight the wide range of spin gap values present in the dataset, underscoring the challenge for any ML model to accurately capture this diversity.

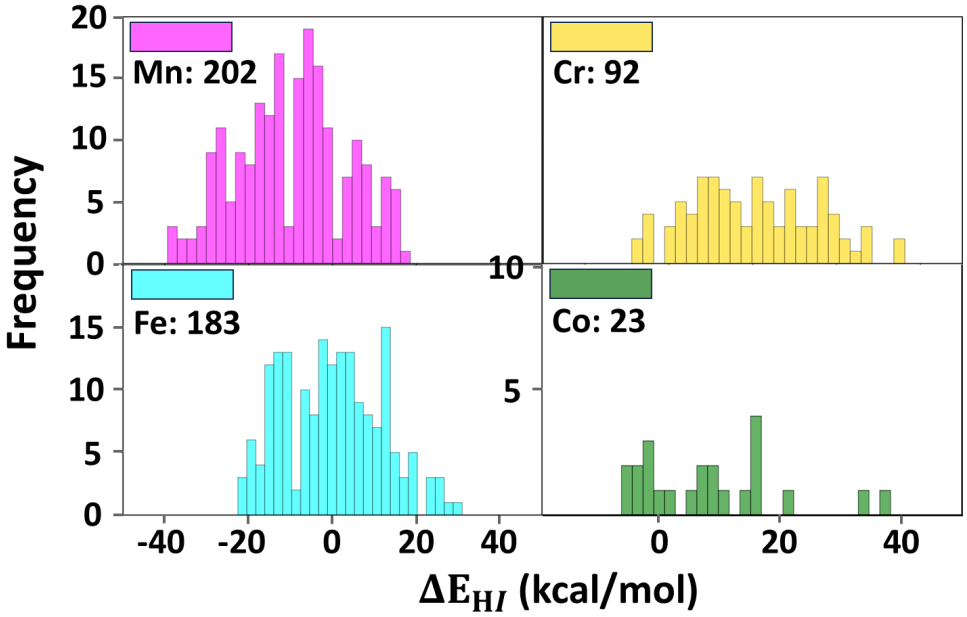

Figure S8: The distribution of B3LYP/def2-TZVP calculated ΔE_{HI} spin gap for four metal centers.

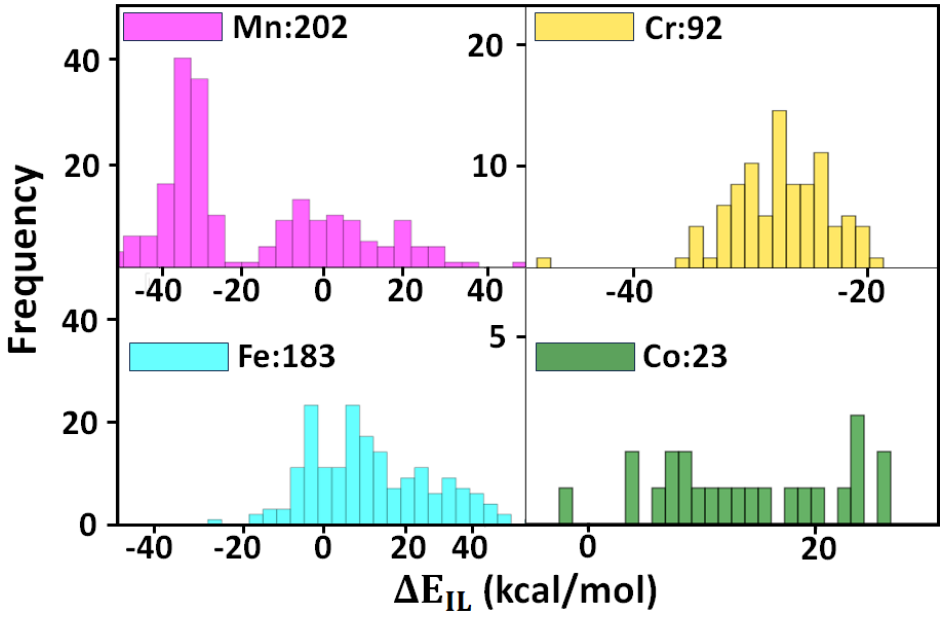

Figure S9: The distribution of B3LYP/def2-TZVP calculated ΔE_{IL} spin gap for four metal centers.

Analysis of adiabatic spin energy gaps (prediction)

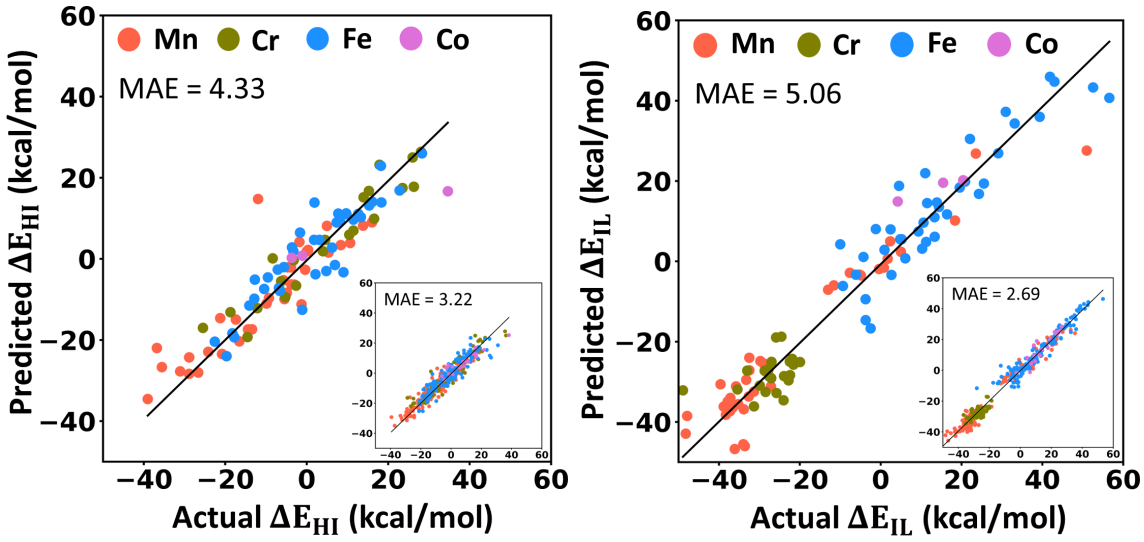

(a) (b)

Figure S10: The correlation plot of actual vs. predicted adiabatic (a) ΔE_{HI} and (b) ΔE_{IL} energy gap, both for the training (inset) and testing dataset using the RAC descriptor. The MAEs are in kcal/mol.

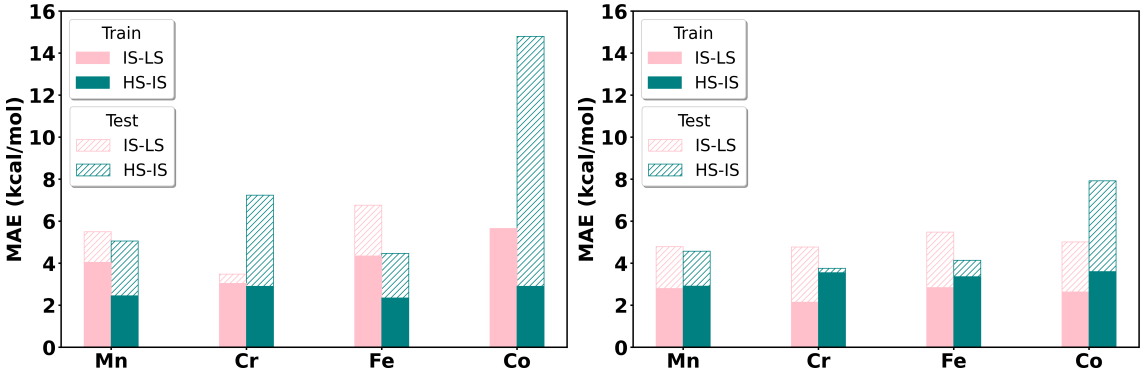

(a) (b)

Figure S11: The MAE of four metal centers in predicting the adiabatic ΔE_{HI} and ΔE_{IL} energy gap using (a) Des-δ and (b) RAC. The MAEs are in kcal/mol.

Fig. S10 shows the comparison of the predicted and calculated spin gaps using RAC. It shows reasonable errors and good correlation for prediction. We further analyze the errors due to each of the metal centers (Fig. S11). The testing error for all the metals except Co is quite impressive. In the case of Co, we obtain quite high errors in prediction. This may

be because the data set comprises only a few Co-containing complexes. Fig. S12 shows the distribution of errors for each metal-centered complex with Des-δ and RAC descriptor. We observe comparable performance from both descriptors.

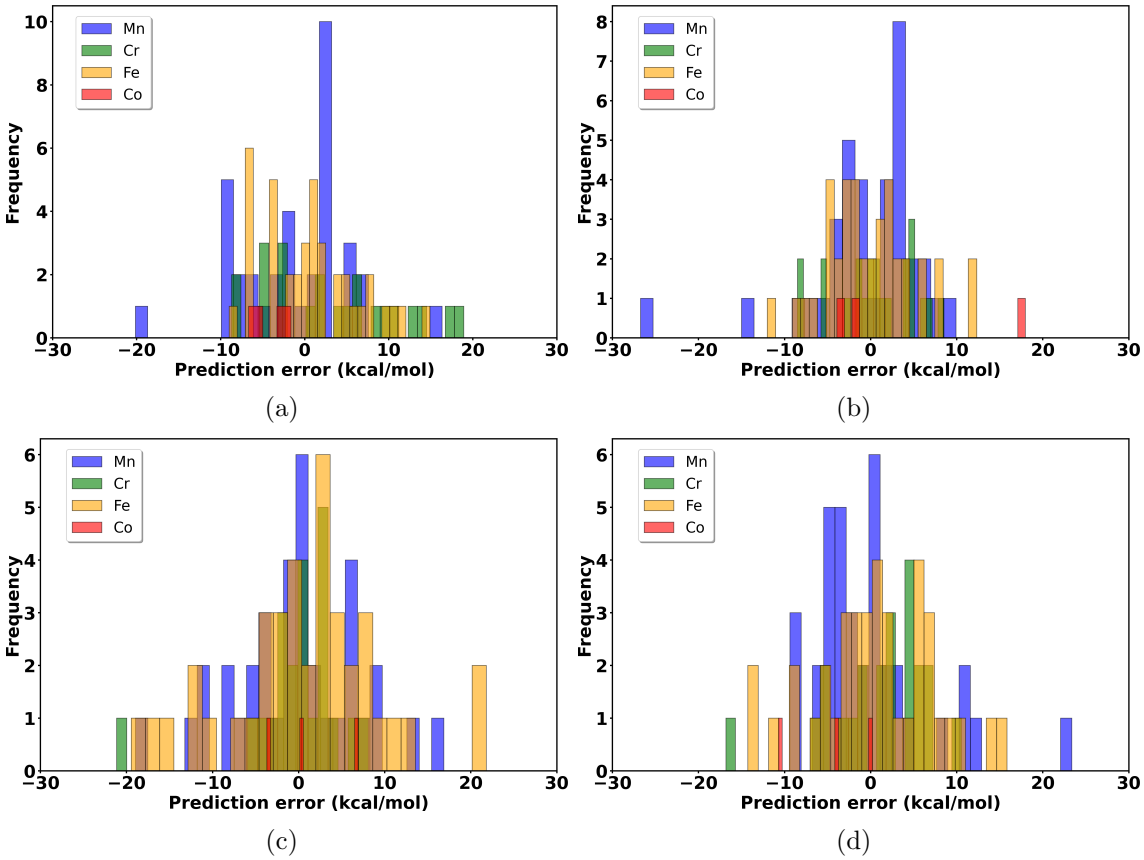

Figure S12: The distribution of prediction error of ΔE_{HI} using (a) Des-δ and (b) RAC for four metal centers. The distribution of prediction error of ΔE_{IL} using (c) Des-δ and (d) RAC. For both descriptors, the maximum error is above 20 kcal/mol.

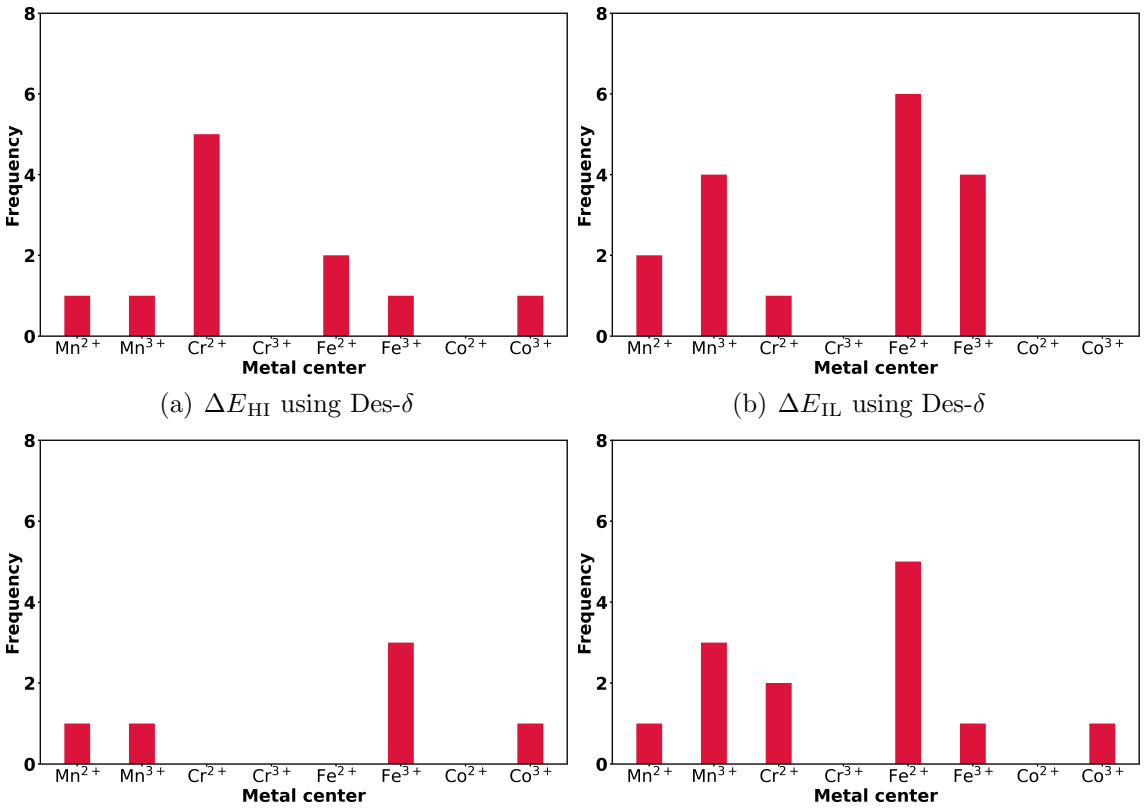

(a) ΔE_{HI} using Des-δ (b) ΔE_{IL} using Des-δ

(c) ΔE_{HI} using RAC (d) ΔE_{IL} using RAC

Figure S13: The distribution of poorly predicted complexes (MAE $\geq$ 10 kcal/mol) for (a) ΔE_{HI} using Des-δ, (b) ΔE_{IL} using Des-δ, (c) ΔE_{HI} using RAC, and (d) ΔE_{IL} using RAC.

Relative importance of input descriptors

To understand the relative importance of each input descriptor, SHAP (Shapley Additive Explanations) analysis was performed for both the spin gap models (HI and IL). No clear indication was observed that could help us determine the least important descriptors with confidence.

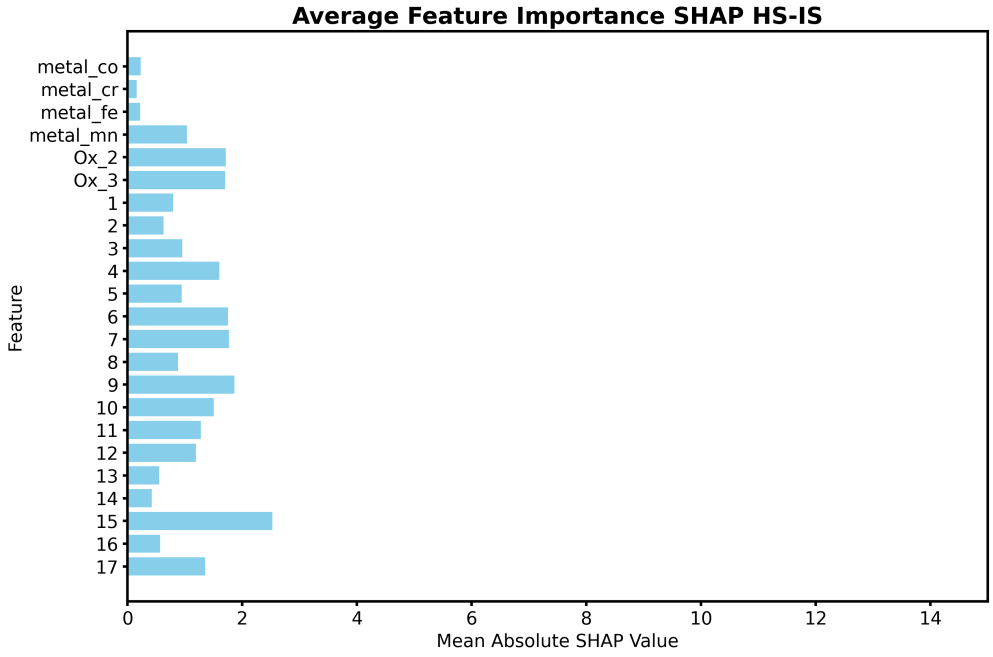

(a)

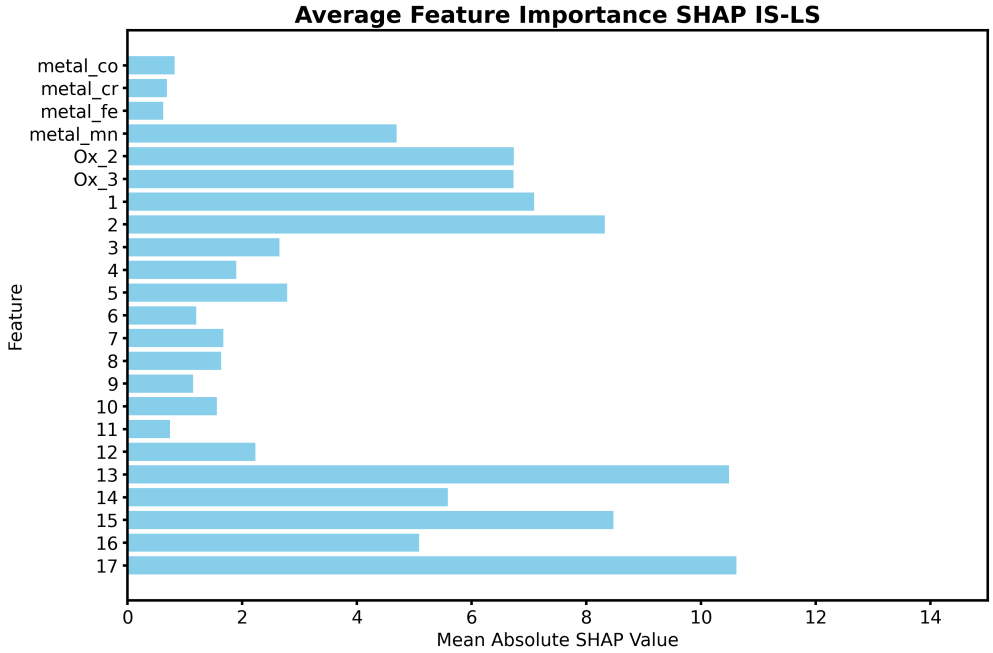

(b)

Figure S14: SHAP (Shapley Additive Explanations) analysis of KRR predictions (a) for ΔE_{HI} gap and (b) ΔE_{IL} gap. The Y-axis shows all the descriptors. The X-axis represents the contribution of each feature in the prediction. The feature numbers correspond to the following classes: 1–5 (5 α d-orbital energies), 6 (natural charge of metal), 7–12 (natural charges of 6 coordinating atoms), 13–17 (5 atomic energies of bare metal ions).

Analysis of adiabatic spin gap prediction from separate models for four metals

The training and testing performance of the KRR model using the Gaussian kernel and Des-δ (without metal name) for each metal is shown in Table-S7. Here, the descriptor size is 19. For Mn, Fe, and Cr, the dataset sizes are sufficient to enable effective model training and testing, resulting in a good correlation between the predicted spin gaps and the reference B3LYP/def2-TZVP spin gaps. In contrast, the dataset for Co is relatively small (only 23), leading to overfitting during training and reduced generalization performance on the test set, as shown in Fig.S15.

Table S7: Train and test MAE errors from four individual models for four metal centers.

Dataset	HS-IS		IS-LS	
	Train MAE (kcal/mol)	Test MAE (kcal/mol)	Train MAE (kcal/mol)	Test MAE (kcal/mol)
all metal	2.25	5.60	4.06	5.50
Mn	2.94	4.61	2.11	4.59
Fe	2.58	6.00	3.33	6.06
Cr	4.21	4.67	1.63	3.72
Co	1.17	4.75	0.41	4.90

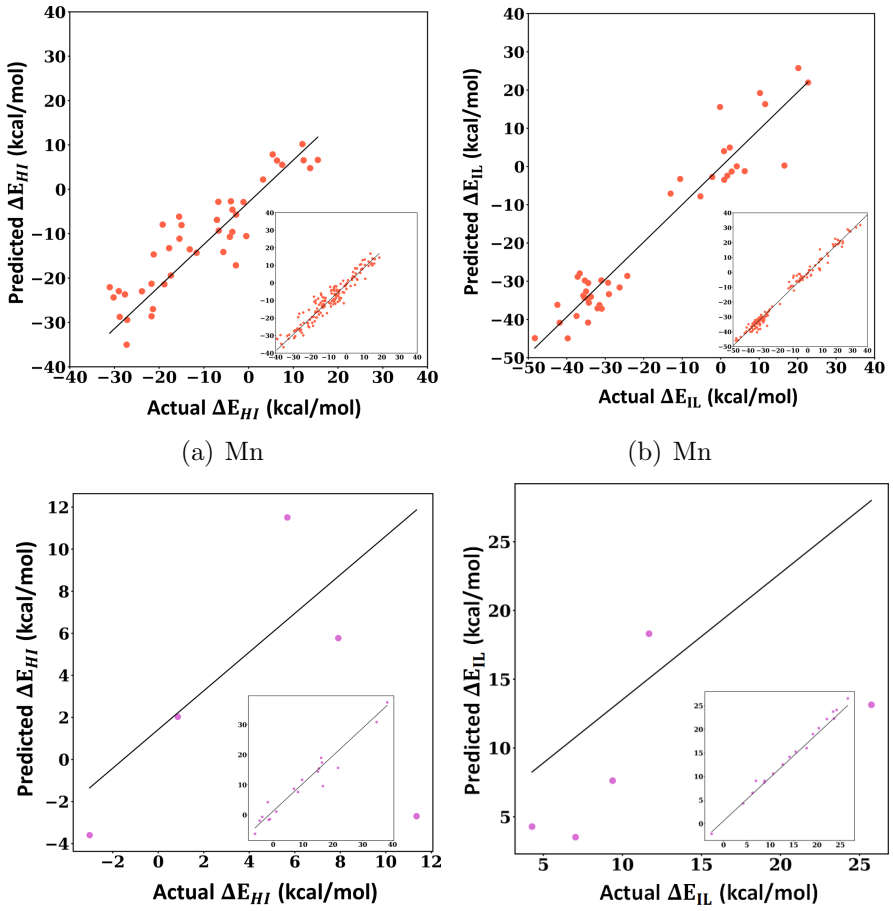

(a) Mn (b) Mn

(c) Co (d) Co

Figure S15: The correlation plot of actual vs. predicted adiabatic ΔE_{IL} and ΔE_{IL} energy gap, both for the training (inset) and testing dataset using Des-δ for individual Mn and Co metal centers.

Analysis of adiabatic spin gap prediction from metal-specific descriptor

Table-S8 presents the training and testing performance of the KRR model using a simplified descriptor that includes only metal-specific information, excluding those information from electronic structure calculation, such as orbital energies or NPA charges. This descriptor consists of 11 features, including one-hot encoded metal identity and oxidation state, along with five energy levels of the corresponding bare metal ions.

Table S8: Training and testing efficiency with descriptor containing only information about metal centers.

	Adiabatic		Vertical	
	Train MAE (kcal/mol)	Test MAE (kcal/mol)	Train MAE (kcal/mol)	Test MAE (kcal/mol)
HS-IS	9.74	11.13	24.87	25.20
IS-LS	8.20	8.55	11.45	12.56

Distribution of B3LYP/def2-TZVP calculated vertical ΔE_{HI} and ΔE_{IL} gaps

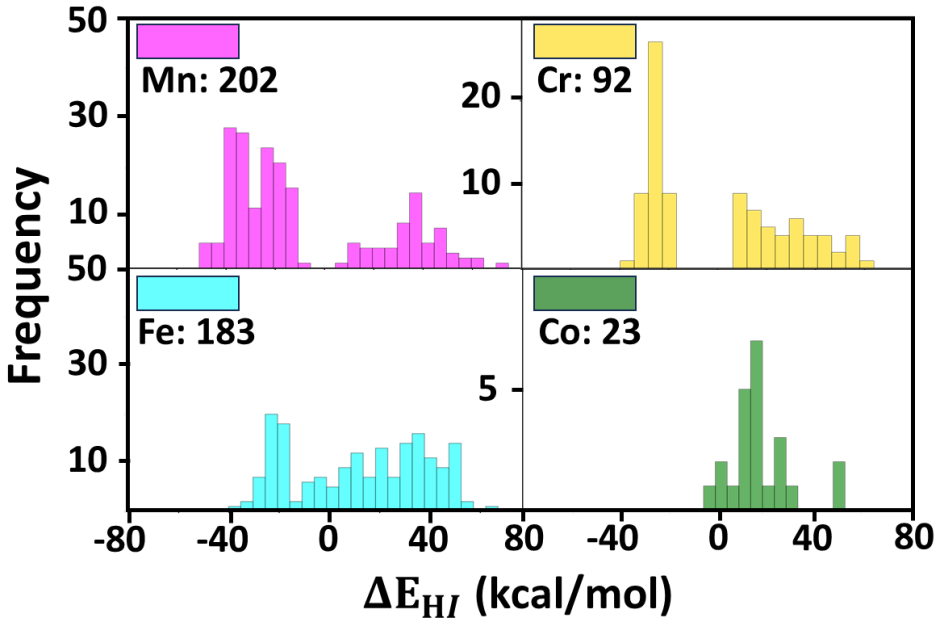

Figure S16: The distribution of B3LYP/def2-TZVP calculated vertical ΔE_{HI} spin gap for four metal centers.

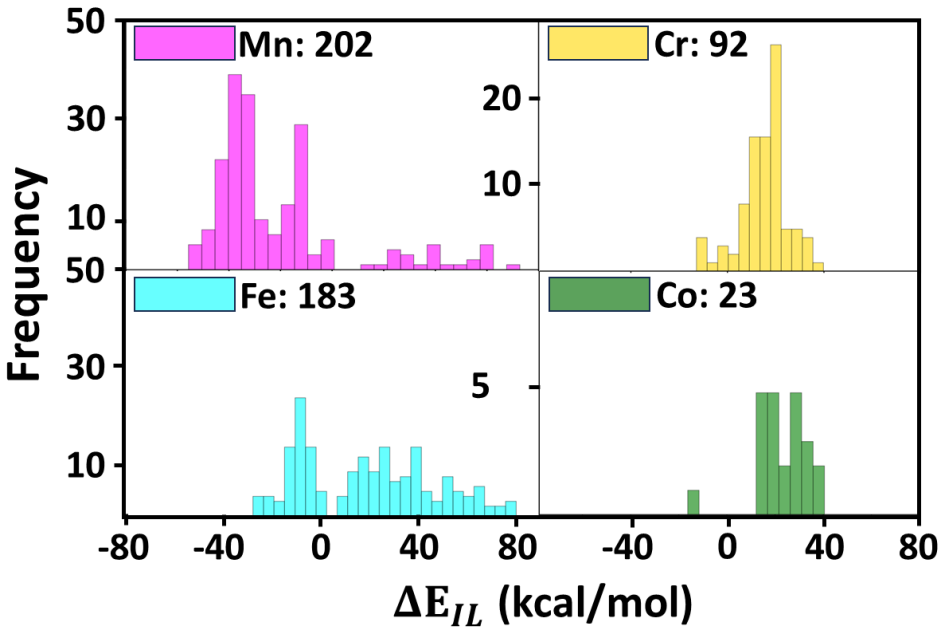

Figure S17: The distribution of B3LYP/def2-TZVP calculated vertical ΔE_{IL} spin gap for four metal centers.

Analysis of vertical spin energy gaps (prediction)

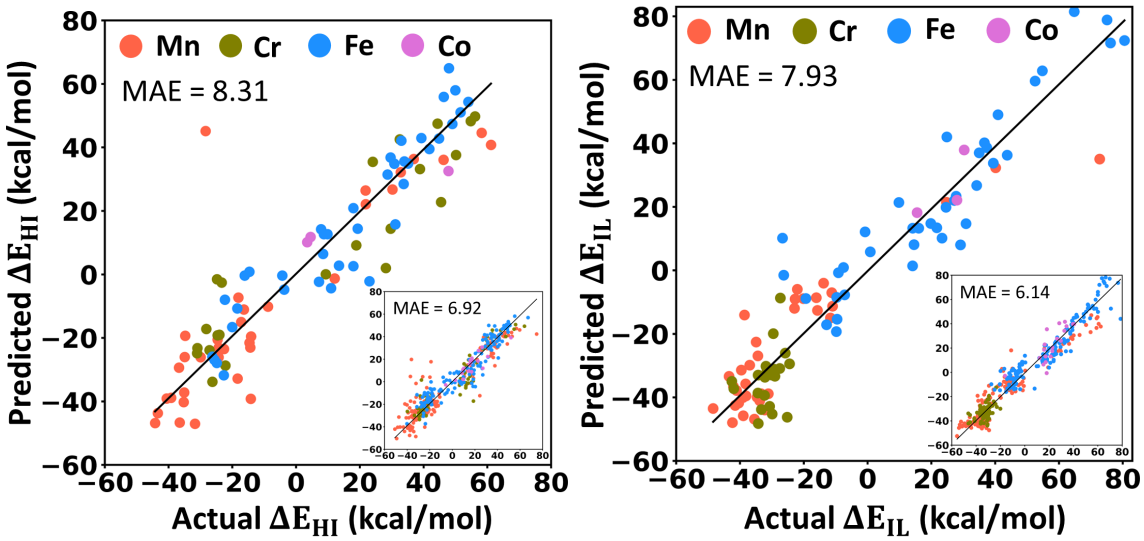

(a) (b)

Figure S18: The correlation plot of actual vs. predicted vertical (a) ΔE_{HI} and (b) ΔE_{IL} energy gap, both for the training (inset) and testing dataset using the RAC descriptor. The MAEs are in kcal/mol.

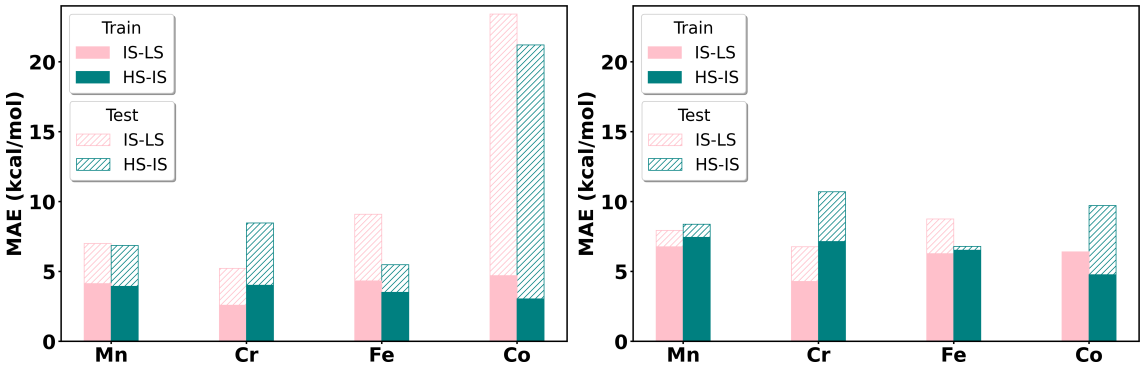

Figure S19: The MAE of four metal centers in predicting the vertical ΔE_{HI} and ΔE_{IL} energy gap using (a) Des-δ and (b) RAC.

Correction to best estimates of spin gaps

The correction factors that need to be added to the B3LYP/def2-TZVP spin gaps to predict more accurate estimates at the CASPT2/CC and PWPB95 levels of theory can also be machine learned efficiently. This is shown in Fig. S20 (the predicted and calculated correction of spin gaps for 50 representative complexes). This prediction is then extended to the full dataset, and we have been able to predict the adiabatic spin gaps for the 500 complexes in the full dataset.

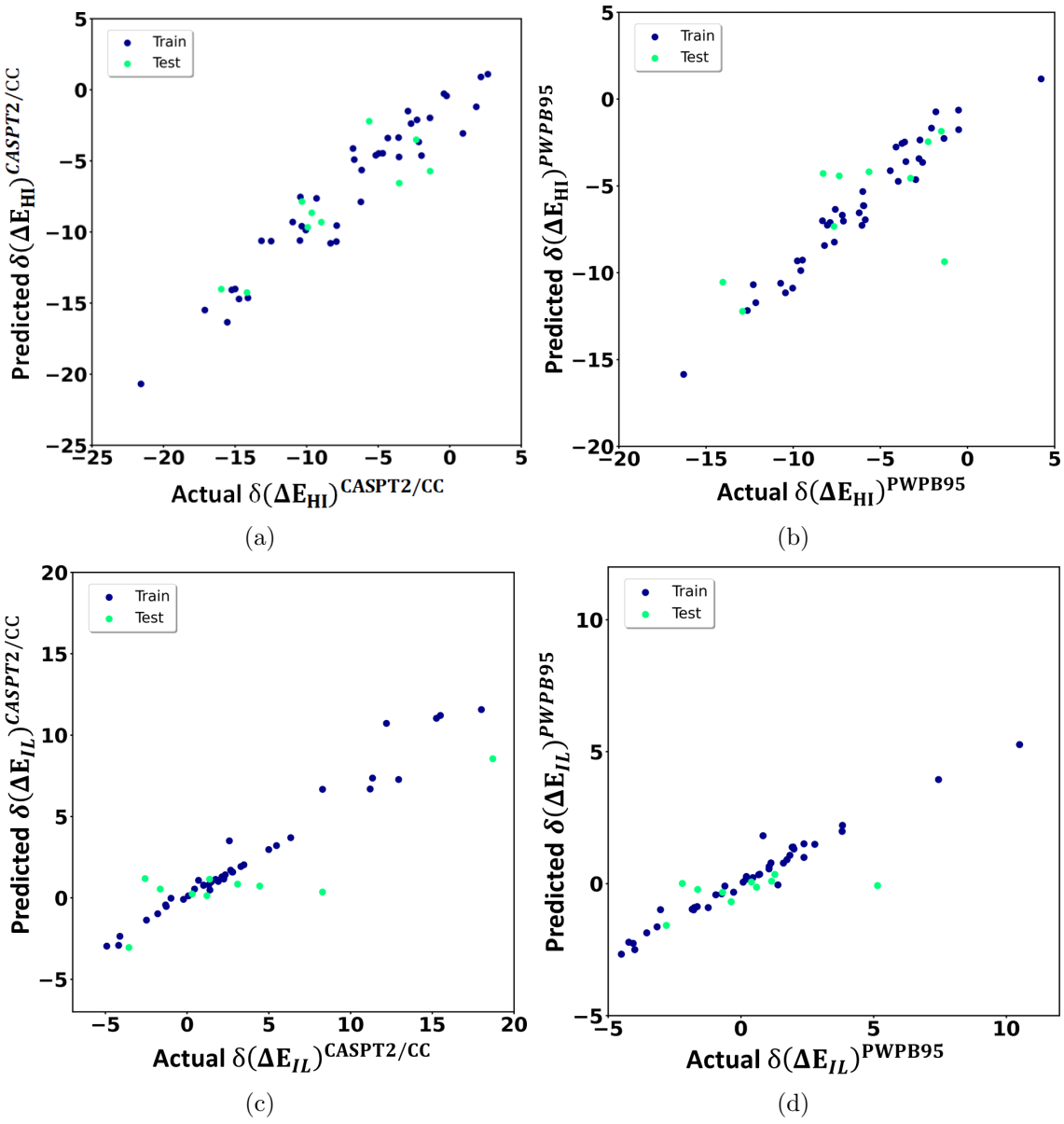

Figure S20: Correlation between predicted and calculated corrections towards best estimate values of spin gap predictions with higher-level methods. (a) Correction of spin gap between high and intermediate spin states (CASPT2/CC). (b) Correction of spin gap between high and intermediate spin states (PWPB95). (c) Correction of spin gap between intermediate and low spin states (CASPT2/CC). (d) Correction of spin gap between intermediate and low spin states (PWPB95). All the corrections are in kcal/mol.

Adiabatic spin gaps predicted at the CASPT2/CC level of theory are shown in Fig. S21.

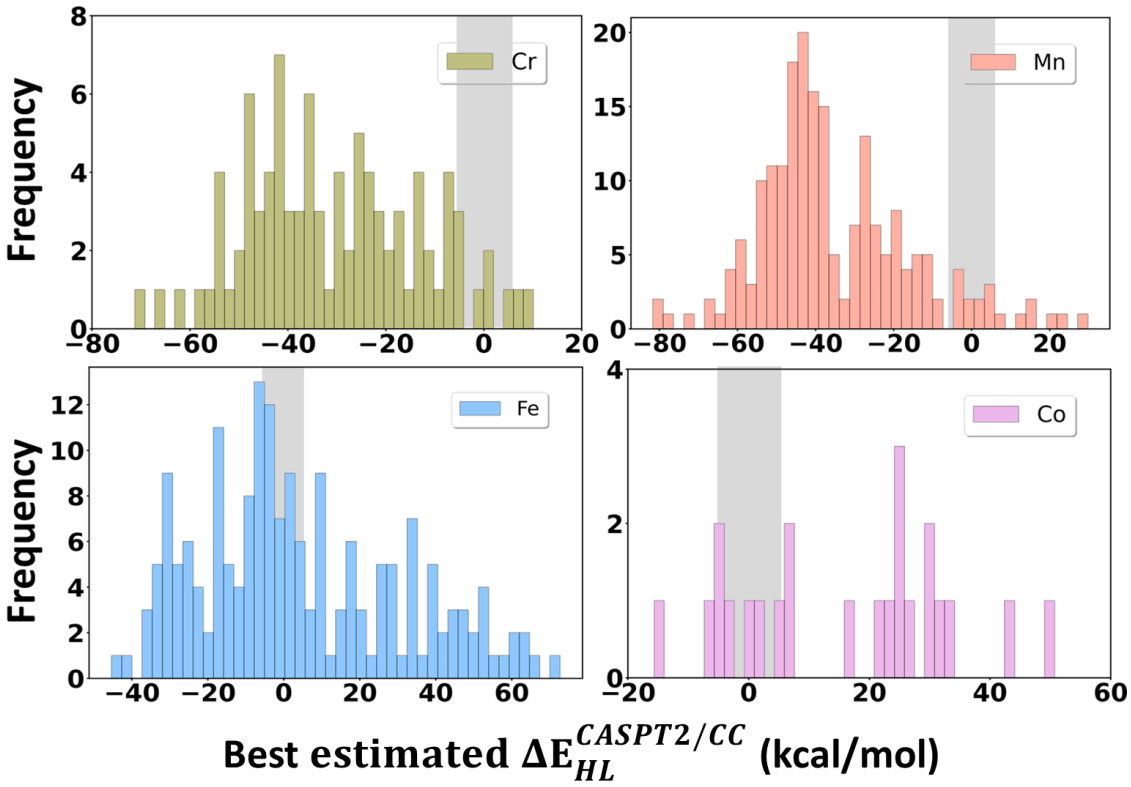

Figure S21: Best estimate of adiabatic spin gaps at CASPT2/CC level of theory. The distribution of best estimated spin gaps ΔE_{HL} for each metal-centered complex is shown separately. The region that would be important in spin crossover phenomena is also marked.

Structures of bimetallic transition metal complexes

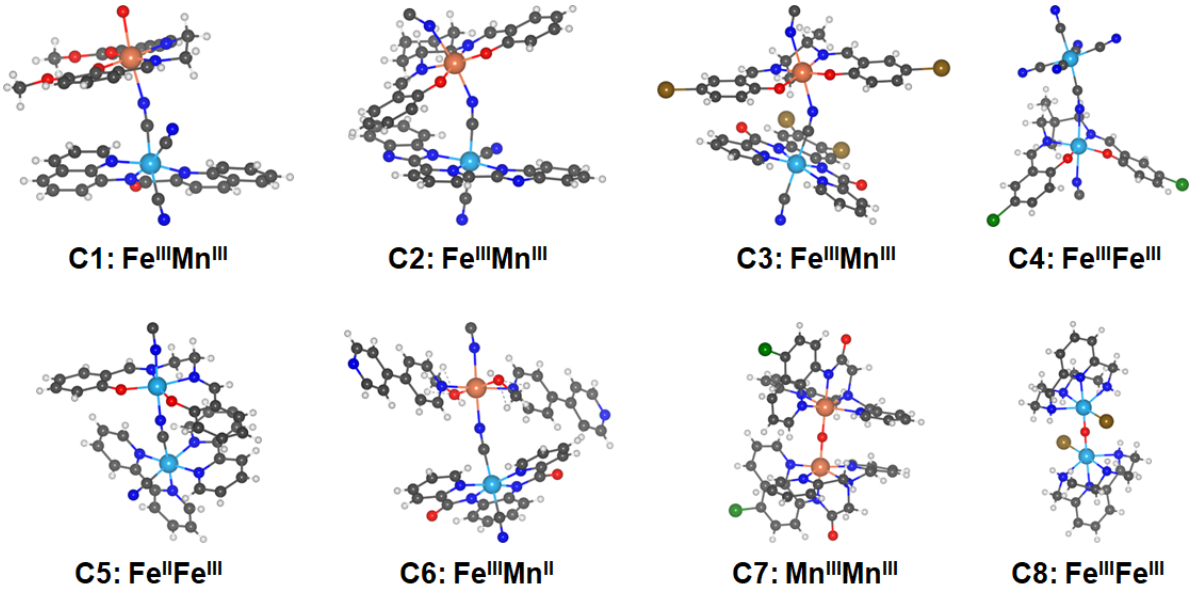

Figure S22: Structure of octahedral monometallic complexes in the dataset.

Protocol of predicting GS spin of each metal core of bimetallic complexes

The protocol of predicting the spin energy gaps of individual metal centers in bimetallic systems is shown in Fig. S23. Initial geometries of these complexes were obtained from experimental X-ray crystallographic data. Each bimetallic complex was systematically divided into two monomeric units by cleaving the bridging ligands between the two metal centers. To maintain chemical stability of the fragmented structures, the valency of the atoms at the cleavage sites was satisfied by capping them with H atoms.

To predict the spin energy gaps of each monomeric fragment, the descriptors for each fragment were subsequently generated via single-point energy calculations at the B3LYP*/def2-SVP level of theory. The ML model, originally trained on the vertical spin-state energy gaps of monometallic complexes, was then applied to predict the spin gaps of each fragment derived from the bimetallic system.

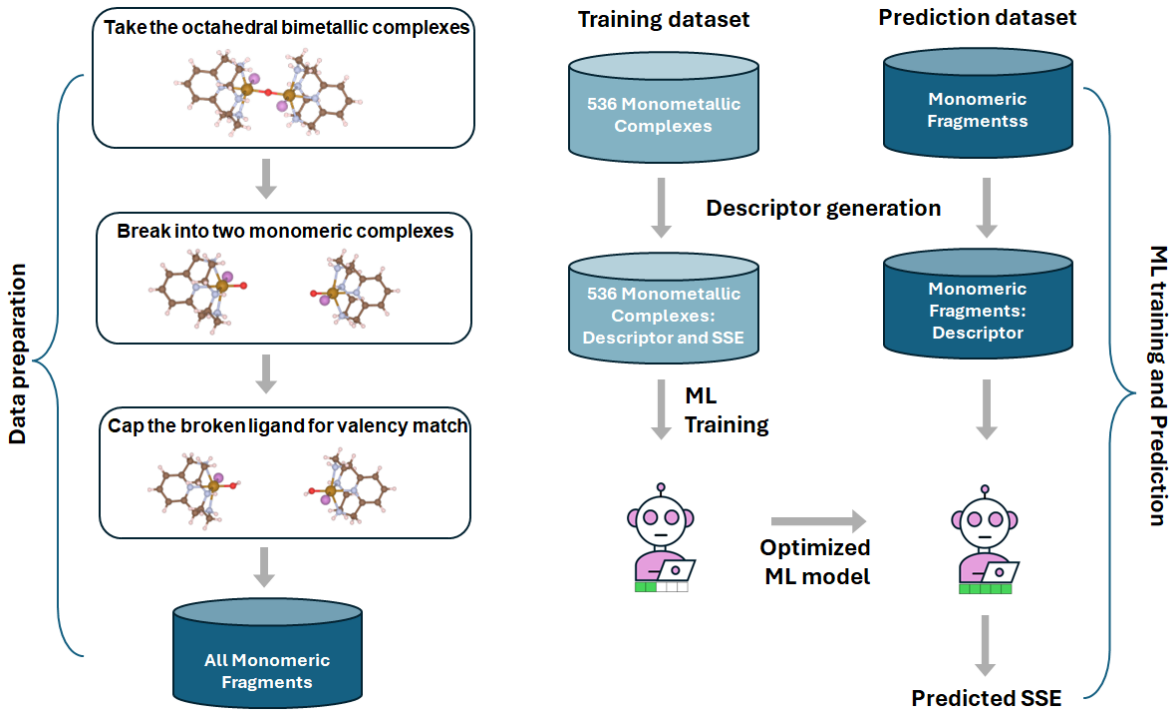

Figure S23: The protocol of predicting spin energy gaps of monomeric units obtained from bimetallic complexes.

Extension to binuclear TM complexes

With the success of the protocol in predicting the GS of mononuclear complexes, we extended the protocol to predict the spin gaps and GS spins of the *individual* metal cores of the binuclear complexes.

Each metal center in a binuclear complex can possess a distinct spin configuration depending on its oxidation state, ligand environment, and local geometry. The individual spin of the metal centers can significantly affect key properties such as redox behavior, electronic communication between centers, and catalytic efficiency.[? ? ?] These local spin states interact through exchange coupling, which can result in a range of global spin states for the complex.

A molecular set of 8 binuclear complexes with octahedral coordination at each metal center was curated from available X-ray crystallographic structures.[2–13] It contains Mn and Fe with +2 and +3 oxidation and coordinates with multidentate ligands as illustrated in Fig. S22. Each binuclear complex was systematically divided into two monomeric units

by cleaving the bridging ligands between the two metal centers. To maintain the chemical stability of the fragmented structures, the valency of the atoms at the cleavage sites was satisfied by capping them with H atoms. Thus, a total of 16 monomeric fragments were generated by cleaving the bridging ligands that connect the two metal centers. The protocol of predicting spin state at individual metal centers in binuclear systems is described in Fig. S23.

KRR models trained on the vertical spin gaps of 500 mononuclear complexes were employed to predict the spin gaps of the fragments. The MAE of the predicted spin gaps for the fragments is 10–17 kcal/mol for both Des-δ and RAC when compared with B3LYP/def2-TZVP reference data (Table S9). It is to be noted that large errors are observed for spin gaps when the training is performed on monodentate ligands and testing is performed on multidentate ligands. More diversification of the training dataset is likely to enhance the accuracy of the spin energy gap.

On the other hand, the predicted GS spin for the individual metal cores (versus B3LYP*) is significantly better. It is correctly predicting the GS spin for 15 metal cores out of 16. Only a single discrepancy was observed for a fragment of one complex containing the Fe metal coordinated with multidentate ligands. Comparison with the experimentally determined spin state (Table S10) shows no inconsistencies, further validating the predictive capability of the ML protocol.

Table S9: MAE (in kcal/mol) and R^2 score of training and testing data. Training data contains 500 monometallic complexes with monodentate ligands, and test data contains 16 fragments.

ΔE	Des-δ				RAC			
	Train MAE	Test MAE	Train R^2 score	Test R^2 score	Train MAE	Test MAE	Train R^2 score	Test R^2 score
ΔE_{HI}	4.99	9.61	0.95	0.73	8.83	9.17	0.84	0.84
ΔE_{IL}	6.25	17.73	0.93	0.43	4.99	14.92	0.95	0.58

Table S10: Comparison of the predicted GS from ML-predicted spin gaps for individual fragments with those obtained from DFT calculations and experimental observations.

Complex	Experimentally observed	Calculated (B3LYP/Def2-TZVP)	Des-δ predicted	RAC predicted
C1_1Fe_3	2	2	2	2
C1_2Mn_3	5	5	5	5
C2_1Fe_3	2	2	2	2
C2_2Mn_3	5	5	5	5
C3_1Fe_3	2	2	2	2
C3_2Mn_3	5	5	5	5
C4_1Fe_3	2	2	2	2
C4_2Fe_3	6	4	6	6
C5_1Fe_2	1	1	1	1
C5_2Fe_3	6	6	6	6
C6_1Fe_3	2	2	2	2
C6_2Mn_2	6	6	6	6
C7_1Mn_3	5	5	5	5
C7_2Mn_3	5	5	5	5
C8_1Fe_3	—	6	6	6
C8_1Fe_3	—	6	6	6

Table S11: Optimal hyperparameters for different spin gap predictions. The hyperparameters were obtained from grid searches over 1 to 10^{-7} with 63 logspace spacing.

	Spin gap	Des-δ		RAC	
		Regularization parameter α	Kernel width γ	Regularization parameter α	Kernel width γ
Adiabatic spin gap	ΔE_{HI}	$5e^{-2}$	$6e^{-2}$	$1e^{-7}$	$8e^{-6}$
	ΔE_{IL}	$8e^{-4}$	$3e^{-3}$	$1e^{-7}$	$3e^{-5}$
Vertical spin gap	ΔE_{HI}	$4e^{-2}$	$5e^{-2}$	$1e^{-7}$	$6e^{-6}$
	ΔE_{IL}	$6e^{-4}$	$6e^{-3}$	$1e^{-7}$	$1e^{-5}$
Fragment spin gap	ΔE_{HI}	$6e^{-2}$	$3e^{-2}$	$1e^{-1}$	$2e^{-3}$
	ΔE_{IL}	$3e^{-6}$	$1e^{-4}$	$6e^{-3}$	$4e^{-3}$
$\delta(\Delta E)^{\mathrm{CASPT2/CC}}$	ΔE_{HI}	$1e^{-3}$	$1e^{-3}$	–	–
	ΔE_{IL}	$6e^{-1}$	$2e^{-1}$	–	–
$\delta(\Delta E)^{\mathrm{PWPB95}}$	ΔE_{HI}	$9e^{-5}$	$4e^{-4}$	–	–
	ΔE_{IL}	$9e^{-1}$	$4e^{-1}$	–	–

References

(1) Drabik, G.; Radoń, M. Approaching the complete basis set limit for spin-state energetics of mononuclear first-row transition metal complexes. *Journal of Chemical Theory and Computation* **2024**, *20*, 3199–3217.

(2) Yao, M.-X.; Zheng, Q.; Cai, X.-M.; Li, Y.-Z.; Song, Y.; Zuo, J.-L. Chiral cyanide-bridged CrIII–MnIII heterobimetallic chains based on [(Tp) Cr (CN) 3]-: synthesis, structures, and magnetic properties. *Inorganic Chemistry* **2012**, *51*, 2140–2149.

(3) Kim, J. I.; Kwak, H. Y.; Yoon, J. H.; Ryu, D. W.; Yoo, I. Y.; Yang, N.; Cho, B. K.; Park, J.-G.; Lee, H.; Hong, C. S. Cyanide-bridged FeIII- MnIII bimetallic complexes with dimeric and chain structures constructed from a newly made mer-Fe tricyanide: Structures and magnetic properties. *Inorganic chemistry* **2009**, *48*, 2956–2966.

(4) Zhang, D.; Zhuo, S.; Zhang, H.; Wang, P.; Jiang, J. Synthesis, crystal structures and magnetic properties of mer-cyanideiron (III)-based 1D heterobimetallic cyanide-bridged chiral coordination polymers. *Dalton Transactions* **2015**, *44*, 4655–4664.

(5) Zhang, D.; Zhuo, S.; Wang, P.; Chen, X.; Jiang, J. A new series of cyanide-bridged heterobimetallic Fe III–Fe III/Mn III/Cu II one-dimensional complexes: Synthesis, crystal structures, and magnetic properties. *New Journal of Chemistry* **2014**, *38*, 5470–5479.

(6) Gungor, E.; Yahsi, Y.; Kara, H.; Caneschi, A. The first 3D and trinuclear cyano-bridged Fe III–Fe III (CN) 6 complexes: structure and magnetic characterizations. *CrystEngComm* **2015**, *17*, 3082–3088.

(7) Zhang, Q.; Zhou, H.; Shen, X.; Zhou, H.; Yang, Y. Syntheses, crystal structures and magnetic properties of four cyano-bridged bimetallic alternating chain complexes based on [Cr III (salen)(CN) 2]- and [Cr III (bipy)(CN) 4]- building blocks. *New Journal of Chemistry* **2013**, *37*, 941–948.

(8) Wang, Y.; Ma, X.; Hu, S.; Wen, Y.; Xue, Z.; Zhu, X.; Zhang, X.; Sheng, T.; Wu, X. Syntheses, crystal structures, MMCT and magnetic properties of four one-dimensional cyanide-bridged complexes comprised of M II–CN–Fe III (M= Fe, Ru, Os). *Dalton Transactions* **2014**, *43*, 17453–17462.

(9) Lan, W.; Zhou, Z.; Li, J.; Dou, Y.; Hao, X.; Yang, L.; Liu, H.; Li, D.; Liu, Q.; Zhang, D. A cyanide-bridged FeIII–MnII heterobimetallic one-dimensional coordination polymer: synthesis, crystal structure, experimental and theoretical magnetism investigation. *Crystal Structure Communications* **2019**, *75*, 1475–1481.

(10) Field, L. D.; Guest, R. W.; Turner, P. Mixed-valence dinitrogen-bridged Fe (0)/Fe (II) complex. *Inorganic chemistry* **2010**, *49*, 9086–9093.

(11) Rice, D. B.; Munasinghe, A.; Grotemeyer, E. N.; Burr, A. D.; Day, V. W.; Jackson, T. A. Structure and reactivity of (μ-Oxo) dimanganese (III, III) and mononuclear hydroxomanganese (III) adducts supported by derivatives of an amide-containing pentadentate ligand. *Inorganic Chemistry* **2018**, *58*, 622–636.

(12) Morsing, T. J.; Bendix, J.; Weihe, H.; Døssing, A. Oxo-bridged dinuclear chromium (III) complexes: Correlation between the optical and magnetic properties and the basicity of the oxo bridge. *Inorganic Chemistry* **2014**, *53*, 2996–3003.

(13) Panza, N.; di Biase, A.; Caselli, A. Structural and spectroscopical characterization of μ-oxo bridged Iron (III) bromide complexes of Pyclen ligands. *Inorganica Chimica Acta* **2022**, *541*, 121091.